

Automatic Target Recognition of SAR Images Based on Global Scattering Center Model

Zhou Jianxiong, Shi Zhiguang, Cheng Xiao, and Fu Qiang

Abstract—This paper proposes a synthetic aperture radar (SAR) automatic target recognition approach based on a global scattering center model. The scattering center model is established offline using range profiles at multiple viewing angles, so the original data amount is much less than that required for establishing SAR image templates. Scattering center features at different target poses can be conveniently predicted by this model. Moreover, the model can be modified to predict features for various target configurations. For the SAR image to be classified, regional features in different levels are extracted by thresholding and morphological operations. The regional features will be matched to the predicted scattering center features of different targets to arrive at a decision. This region-to-point matching is much easier to implement and is less sensitive to nonideal factors such as noise and pose estimation error than point-to-point matching. A matching scheme going through from coarse to fine regional features in the inner cycle and going through different pose hypotheses in the outer cycle is designed to improve the efficiency and robustness of the classifier. Experiments using both data predicted by a high-frequency electromagnetic (EM) code and data measured in the MSTAR program verify the validity of the method.

Index Terms—Ground target, model based, scattering center, synthetic aperture radar (SAR) automatic target recognition (ATR).

I. INTRODUCTION

AUTOMATIC target recognition (ATR) of synthetic aperture radar (SAR) targets (abbreviated as SAR ATR in the following) is essential in better exploring large SAR images. An integrated SAR ATR system may consist of three stages: detection, discrimination, and classification [1], [2]. The first two stages will reject the clutter false alarms and will select out the image chips, i.e., regions of interest (ROIs), containing candidate targets. The ROIs are sent to the third stage (classifier) to decide the target type. In this paper, we will propose a model-based classifier for the third stage based on a global scattering center model.

ATR classifiers can be categorized into two types: template or model based [1]. Template-based classifiers maintain a large database of exemplar feature vectors or templates, taken from

images of targets in the library at a number of different poses. Candidate targets are classified based on how well their images or features match the templates in the database. Lincoln Laboratory's ATR system SAIP is a typical template-based one where each template abstracts the target features in a scope of 5° [2]–[4]. Model-based classifiers maintain a database of physical or conceptual models of targets to predict features at different poses and deployment conditions online. They are called feature-based classifiers in [5] since the physical models are regarded as features extracted from the original data that greatly reduce the data dimension. There are also statistical-model-based classifiers where the features of different targets are modeled as statistical processes with different parameters [6]–[8]. The ATR system developed in the MSTAR program uses a typical model-based classifier in which scattering centers extracted from 3-D CAD models drive the prediction of SAR image features [9]–[11]. In recent years, there has been a surge of interest in model-based ATR systems [1], [9]–[17]. The prominent advantages include a compact database, template prediction in real time for a continuous and arbitrarily fine selection of target pose, flexibility in extended operation conditions [14], etc.

The scattering center model provides a concise and physically relevant description of the target radar signature. Therefore, it is a natural candidate model for model-based SAR ATR [1], [9]–[12], [15]–[17].

There has been much effort to establish scattering center models for ATR usage [1], [18]–[21]. A great difficulty is that radar images are sensitive to target pose, so the scattering centers extracted from one image are only valid in its neighboring angular extent [21]. In [1], [12], [13], and [20], images at every 1° angular interval are used to extract a scattering model, so the original data amount is still very large. In [19], a global scattering center model valid in a large angular extent is established by combining scattering centers extracted from 3-D images at every 3° angular intervals, and the 3-D images are conveniently obtained by exploring the one-look ISAR ability of the shooting and bouncing ray technique. However, this method seems infeasible for measured data or data predicted by other high-frequency electromagnetic (EM) code where 3-D imaging requires a synchronized azimuth-by-elevation aperture with a very large data amount.

Another difficulty in the scattering-center-model-based ATR is what feature to use and how to use it. An unsolved problem is how to get scattering centers from a single SAR image, and any of such points would certainly not be the same as the 3-D ones. Projected 2-D scattering centers can be predicted from a 3-D scattering center model, but to match them with

Manuscript received September 27, 2010; revised May 10, 2011 and July 8, 2011; accepted July 10, 2011. Date of current version September 28, 2011. This work was supported in part by the China National Science Foundation under Grant 60972113.

Z. Jianxiong, S. Zhiguang, and F. Qiang are with the ATR Laboratory, School of Electronics Science and Engineering, National University of Defense Technology, Changsha 410073, China.

C. Xiao is with the Beijing Aerospace Control Center, Beijing 100094, China.

Color versions of one or more of the figures in this paper are available online at <http://ieeexplore.ieee.org>.

Digital Object Identifier 10.1109/TGRS.2011.2162526

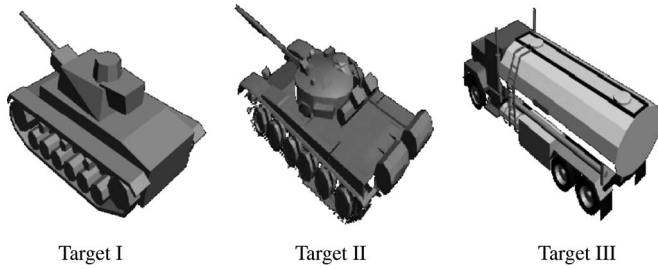


Fig. 2. CAD models of three ground targets.

scattering coefficient not on the grid points can be interpolated from the adjacent grid points.

Fig. 2–4 show the scattering center models for three targets that will be used in Section IV. The scattering center model for a T-72 tank used in Section V will be shown there. The original data are computed by an EM code in the following parameters: frequency from 5 to 6 GHz, with a 12.5-MHz step; azimuth from 0° to 180° , with 1° interval; and elevation from 0° to 80° , with 1° interval. The EM code predicts the radar cross sections (RCS) of complex and electronically large targets based on the high-frequency approximations and the graphical EM computing techniques [23]. Similar approaches are used in other SAR simulators [15], [16], [24]. Several simplifications are assumed in the EM computing: 1) the material of the target is modeled as perfectly conducting; 2) the multiple scatterings among different parts of the target are not considered; 3) the cavities on the target, such as the gun, are obturated; and 4) the backscattering of the ground, together with its interaction with the target, are not computed. Therefore, these effects are not reflected by the scattering center model.

There are 95, 110, and 98 scattering centers in the models for targets I, II, and III, respectively. In Figs. 2 and 3, we can see that their positions coincide with the target structures. Fig. 4 shows the scattering coefficient of the first scattering center of target I. This scattering center is on the front end of the gun, as shown in Fig. 3. It is a very stable scattering center according to its rank [18]. In Fig. 4, we can see that it is always viewable in the front view. Both its amplitude and phase change slowly at different viewing angles.

Although there are nonstable scattering phenomena in real targets, the stable scattering centers are important signatures for recognition [1], [18]–[20], and this will be verified by experiments in Sections IV and V.

Using scattering center models in ATR has other benefits in addition to the advantages of general model-based systems: 1) the scattering center model is not particular to radar system parameters such as the precise operating frequency, bandwidth, and waveform. In Section IV, the scattering center models will be used to classify SAR images at different resolutions, and in Section V, the scattering center model built from C-band EM data will be used to classify SAR image chips measured by an X-band radar. 2) The scattering center model has explicit physical interpretation, so it can incorporate both radar and nonradar information. For example, the positions of some scattering centers can be inferred from the CAD model or target drawing. If the target configuration is changed, relevant

scattering centers can be modified to reflect the change without rebuilding a new model from the beginning.

III. MODEL-BASED SAR ATR APPROACH

The scattering-center-model-based classifier is shown in Fig. 5. In this section, the main steps will be explained with examples.

A. Regional Feature Extraction

The input of the classifier is the image chip containing the target after clutter suppression. Two levels of regional features are extracted from the image chip. Both of them are binary images, i.e., they describe regions without specific amplitude information.

The first level is the coarse regional feature \mathbf{F}_0 which describes the target shape and contour. The extraction algorithm is shown in the left branch of Fig. 6. It is reasonable that bright pixels will be denser on the target than in the background. Therefore, we select the S strongest pixels to ensure that the strong pixels on the target are not missed out. The value for S is determined by the approximate target size, the image resolution, and the pixel size. For example, for the ground targets in Fig. 2, we set $S = 800$ for images at a resolution of $0.15 \text{ m} \times 0.15 \text{ m}$ and $S = 250$ for images at a resolution of $0.3 \text{ m} \times 0.3 \text{ m}$ (the pixel size is slightly smaller than the resolution because of interpolation in image or zero-padding in spectrum). A morphological closed operator is used to connect the dense bright points on the target, whereas the sparse bright points in the background are not affected. A morphological open operator is followed to filter out the sparse bright points in the background and to smooth the target contour. The structuring elements for the morphological operators are empirically selected. In the experiments in Sections IV and V, \mathbf{S}_1 and \mathbf{S}_2 are, respectively, 7×7 and 3×3 all-1 matrices. The definitions of the fundamental morphological operators are given in the Appendix.

The second level is a series of fine regional features \mathbf{F}_n ($n = 1, 2, \dots$) which describe the positions of the strong scatterers on the target. The features are obtained by cutting the image in the coarse regional feature area by different thresholds, as shown in the right branch of Fig. 6. Empirically, we set $th_n = 1 - 0.05(n - 1)$. As n increases, fewer target details are obtained with higher accuracy. Note that, in the second step of Fig. 6 (normalization), the cubic root of the pixel amplitude is used to reduce the dynamic range.

Fig. 7 shows an example of regional features for target II. The original image (the top-left subfigure) is obtained from data predicted by the EM code. The imaging parameters and steps will be elaborated in Section IV. The resolution is about $0.15 \text{ m} \times 0.15 \text{ m}$, and the signal-to-noise ratio (SNR) is 15 dB as defined in (7) in the following. We add additive Gaussian white noise rather than ground clutter, so there is no shadow in the image. In Fig. 7, we can see that the coarse regional feature (\mathbf{F}_0) approximates the target's shape and contour, and the fine regional features $\mathbf{F}_1 - \mathbf{F}_{11}$ retain the positions of the strong scatterers on the target in increasing precision and decreasing

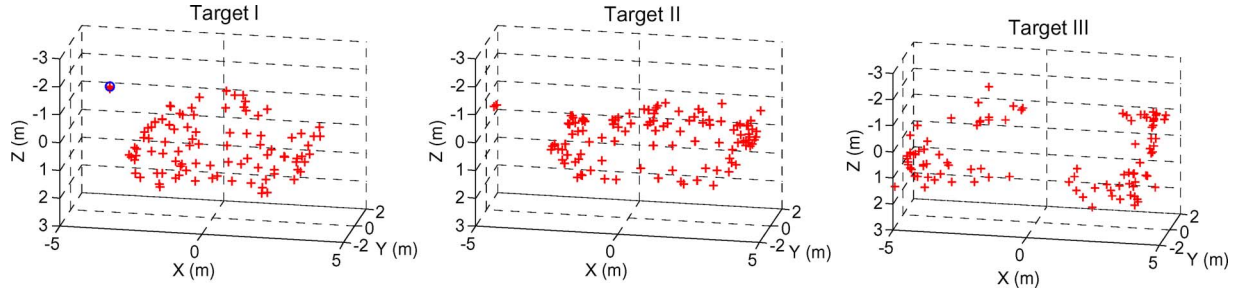


Fig. 3. Scattering center models for the targets in Fig. 2. There are 95, 110, and 98 scattering centers for targets I, II, and III, respectively. “+” indicates the positions of the scattering centers. A blue circle is overlaid on the first scattering center of target I, and its scattering coefficients will be shown in Fig. 4.

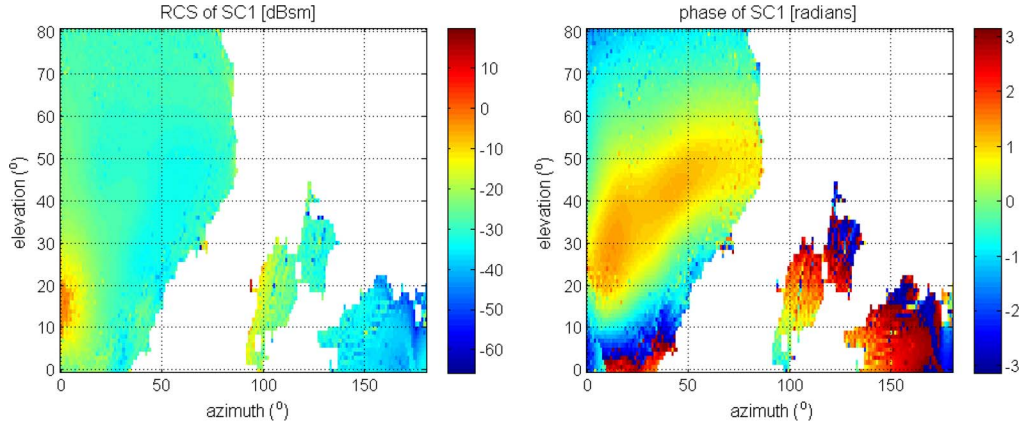


Fig. 4. Scattering coefficients at different azimuth and elevation angles of the first scattering center of target I. The position of this scattering center is marked by a blue circle in Fig. 3. The left subfigure is the intensity of the scattering coefficient ($20 \log_{10} |a_1(\theta_i, \gamma_j)|$). The right subfigure is the phase of the scattering coefficient ($\angle a_1(\theta_i, \gamma_j)$). The white background indicates the angular extent where this scattering center is not viewable.

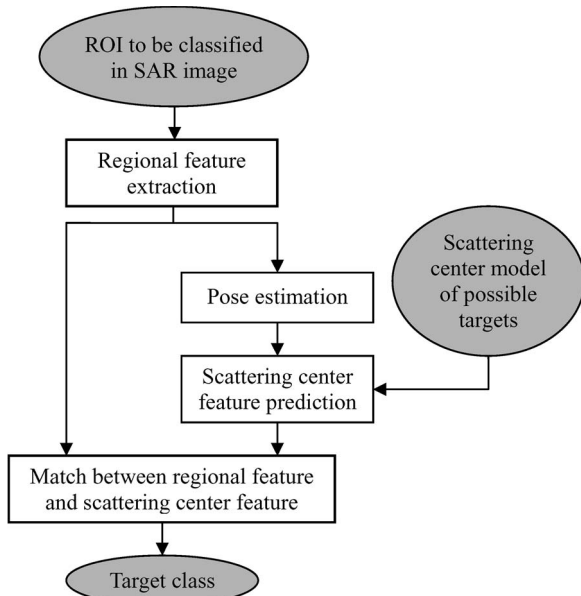


Fig. 5. Scattering-center-model-based SAR classifier.

quantity. Also, we can see that the white pixels in $\mathbf{F}_5 - \mathbf{F}_{11}$ align in the same direction as the pose of the target. Therefore, the fine regional features are also used for pose estimation.

B. Pose Estimation

The target pose can be described by the direction of the radar line of sight (LOS), as shown in Fig. 1. For vehicles on the flat

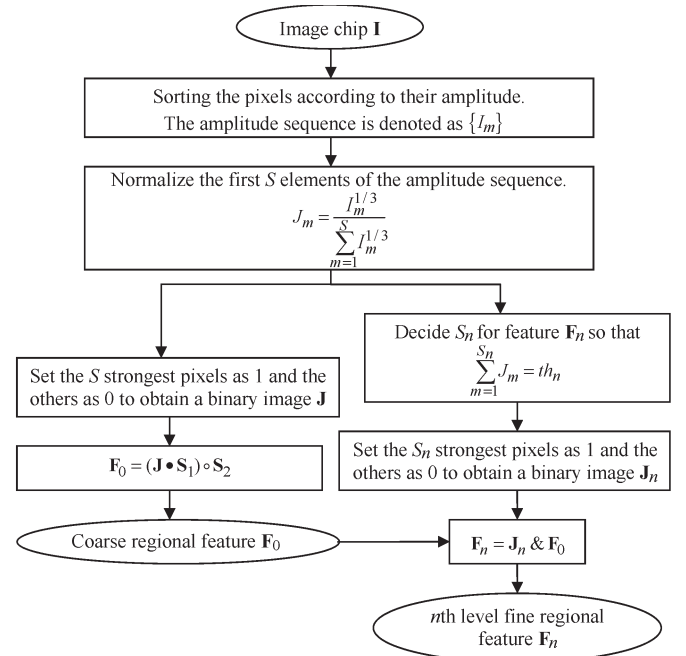


Fig. 6. Regional feature extraction algorithm.

ground, the elevation angle γ can be estimated from the height of the radar platform and its distance to the target. Therefore, the main concern of pose estimation is the azimuth θ , which is also the tilt angle of the target image (the angle between the target main axis and the range axis) in the ground plane.



Fig. 7. Regional features for target II at a center azimuth of 35° and an elevation of 10° . The first row from left to right is the original image (in decibel scale), \mathbf{F}_0 , \mathbf{F}_1 , and \mathbf{F}_3 , respectively. The second row from left to right is \mathbf{F}_5 , \mathbf{F}_7 , \mathbf{F}_9 , and \mathbf{F}_{11} , respectively. In subfigures 2–8, white pixels denote one, and black pixels denote zero.

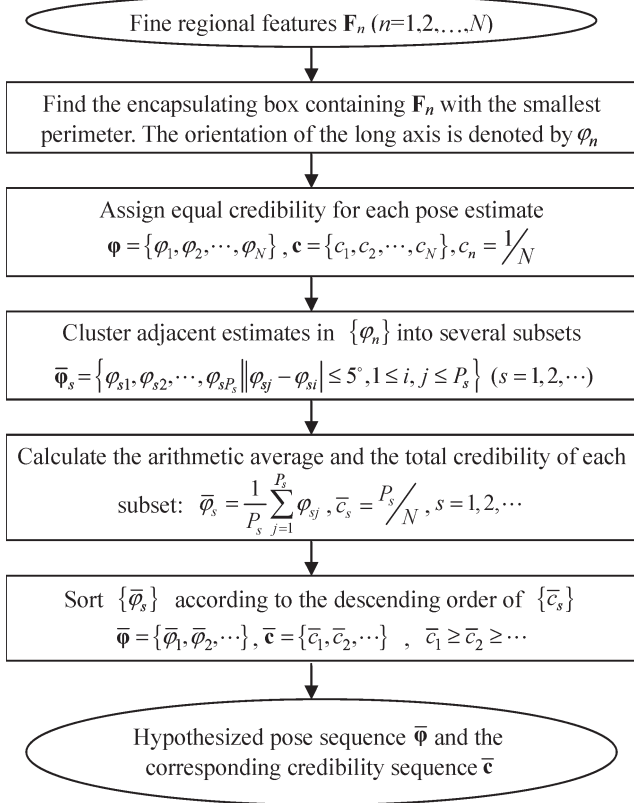


Fig. 8. Pose estimation algorithm.

There are many pose estimation criteria [25], and we select a simple one because of two characteristics of our classifier: 1) the decision mechanism (see Section III-E) will search through a pose sequence. Therefore, it is not required that the pose estimator give the only correct estimate at once. It may give many pose hypotheses descending in credibility (the definition and calculation of the credibility will be given in Fig. 8), and the wrong hypotheses before the correct one will be rejected if they do not produce a satisfying matching score. 2) The region-to-point match is robust to small pose variations, as will be demonstrated in Section III-D. This releases the requirement on the accuracy of the pose estimator. Therefore, we choose the encapsulating box mechanism with the smallest perimeter criterion to estimate target pose.

The pose estimation algorithm is shown in Fig. 8. Using the fine regional features as input avoids additional computation. The estimates for different feature levels (we use $\mathbf{F}_1 - \mathbf{F}_{19}$ in

our experiments) are clustered since small pose variations are tolerable for the following matching step. Clustering also helps in reducing the number of pose hypotheses and in calculating the credibility of each hypothesis.

Fig. 9 shows the intermediate results for pose estimation using the image chip in Fig. 7. The target tilt angle is 35° , and the pose hypotheses after clustering and sorting are $[34^\circ, 26^\circ, 43^\circ, 47^\circ, 70^\circ, 74^\circ, 90^\circ, 105^\circ, 112^\circ]$. The error of the first hypothesis is only -1° .

Fig. 10 shows the pose estimation result for target II at azimuths from 15° to 165° and an elevation of 10° . There is no 180° ambiguity in the results, whereas it is a problem when dealing with ground targets in field data [25]. The image resolution is about $0.15 \text{ m} \times 0.15 \text{ m}$, and the SNR is 10 dB. In Fig. 10, we can see that, in most cases, an estimation error less than 5° can be achieved in the first five hypotheses.

C. Scattering Center Feature Prediction

The 2-D scattering center feature $\mathbf{S} = \{(x''_k, y''_k, A_k), k \in \kappa(\theta, \gamma)\}$ to be matched with the regional feature can be predicted from the 3-D scattering center model in (1) by

$$\begin{bmatrix} x'_k \\ y'_k \end{bmatrix} = \begin{bmatrix} \hat{\mathbf{x}}' \\ \hat{\mathbf{y}}' \end{bmatrix} \mathbf{P}_k = \begin{bmatrix} \cos \gamma \cos \theta & \cos \gamma \sin \theta & \sin \gamma \\ -\sin \theta & \cos \theta & 0 \end{bmatrix} \begin{bmatrix} x_k \\ y_k \\ z_k \end{bmatrix} \quad (2)$$

$$x''_k = \frac{x'_k}{\cos \gamma}, \quad y''_k = y'_k \quad (3)$$

$$A_k = \frac{\Delta \theta}{\Theta} \sum_{|\theta_i - \theta| \leq \frac{\Theta}{2}, \gamma_j = \gamma} |a_{k,i,j}| \quad (4)$$

$$\kappa(\theta, \gamma) = \{k \mid 1 \leq k \leq K, A_k > 0\}. \quad (5)$$

Here, θ is the hypothesized azimuth, and γ is the elevation angle estimated from the SAR geometry. $\hat{\mathbf{x}}'$ and $\hat{\mathbf{y}}'$ are the unit vectors of the range and cross-range axes in the imaging plane. Therefore, x'_k and y'_k indicate the k th scattering center's position in the imaging plane, and x''_k and y''_k indicate its position in the $x''oy''$ coordinate system where the image is mapped back (not projected) to the ground plane. For the geometric relationship between different coordinate systems, please refer to Fig. 1. Θ is the size of the synthetic aperture, and $\Delta \theta$ is

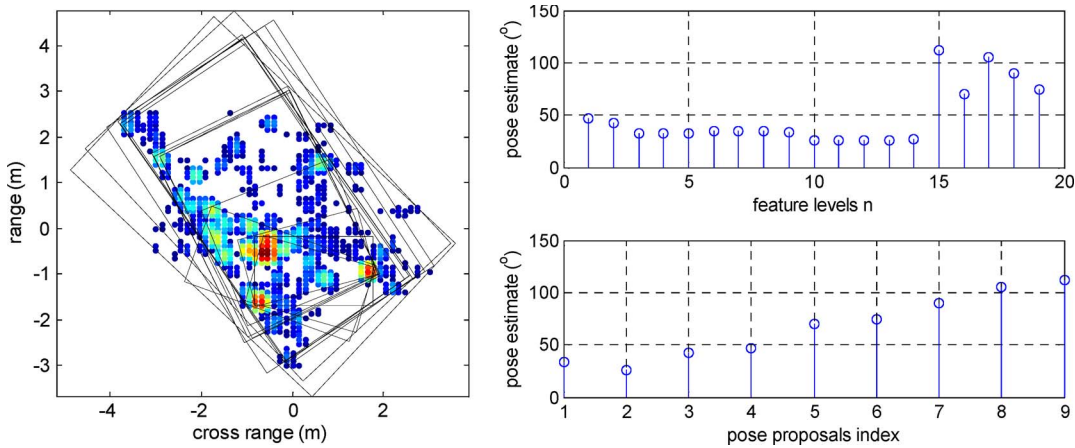


Fig. 9. Pose estimation instance for target II at a center azimuth of 35° and an elevation of 10° . The original image is the same as that in Fig. 7. The left subfigure shows the encapsulating boxes for $F_1 - F_{19}$ (the encapsulating box for F_1 is the outermost one, and that for F_{19} is the innermost one). The image pixels in F_1 are shown by color points in this subfigure. The upper-right subfigure is the tilt angle of each encapsulating box. The bottom-right subfigure is the pose hypotheses after clustering and sorting.

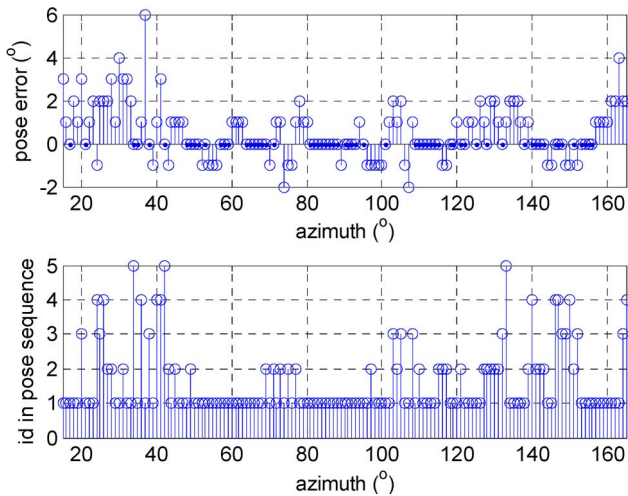


Fig. 10. Pose estimation result for target II at different azimuth angles and elevation of 10° . The first row is the minimum pose error at each azimuth obtained by the first five hypotheses in the pose sequence. The second row is the index of the hypothesis, with the minimum estimation error at each azimuth.

the azimuth angular interval for model building. Therefore, A_k is the averaged amplitude of the k th scattering center in the synthetic aperture. $\kappa(\theta, \gamma)$ is an index set indicating which scattering centers are viewable in this aperture.

Fig. 11 compares the scattering center features of target II with its radar images at different target poses. The resolution is about $0.15 \text{ m} \times 0.15 \text{ m}$, and $\text{SNR} = 15 \text{ dB}$, where the SNR is defined in (7). Since the images are mapped to the ground plane, there is no scaling effect between the images at different elevation angles. However, the resolution in the ground plane will be worse for higher elevation. The predicted scattering centers are overlaid on the image by “+,” with the size proportional to $A_k^{1/3}$. Fig. 11 shows a good correspondence between the predicted scattering center features and the radar images. There are always strong scattering centers in the bright regions of the image. This motivates the design of a matching score between the regional feature and the point feature in the following section.

D. Region-to-Point Matching

The matching score to measure the correspondence between the extracted regional feature F_n ($n = 0, 1, \dots, N$) and the predicted scattering center feature $S = \{(x''_k, y''_k, A_k), k \in \kappa(\theta, \gamma)\}$ is defined as

$$g = s/s_{\text{total}} \quad q = p/Q \quad (6)$$

where $s_{\text{total}} = \sum_{k \in \kappa(\theta, \gamma)} A_k^{1/3}$, $s = \sum_{(x''_k, y''_k) \in F_n} A_k^{1/3}$, $Q = \sum_{k \in \kappa(\theta, \gamma)} 1$, and $p = \sum_{(x''_k, y''_k) \in F_n} 1$.

F_n is a binary matrix describing a region in the image. In a continuous coordinate system, it can also be viewed as an infinite set containing all the points in the region (e.g., the white area in subfigures 2–8 of Fig. 7). s_{total} is the total intensity of the predicted scattering centers, and s is the intensity in the region. Q is the total number of the predicted scattering centers, and p is the number of scattering centers in the region. Therefore, both $0 \leq g \leq 1$ and $0 \leq q \leq 1$ indicate how well the predicted feature fits the regional feature. Since the dynamic range of A_k is always very large (tens of decibels), a few very strong scattering centers in the region will result in a high matching score even if the others are not in the region. Therefore, we use the cubic root of A_k to reduce the dynamic range, and the score q is an extreme case of dynamic range reducing where all the scattering centers are equally weighted. Both g and q will be used in the decision procedure.

Now, we give several examples to illustrate the characteristics of the region-to-point matching: 1) both the feature extraction and the matching use simple mathematical operations. Fig. 12 compares the region-to-point match with the point-to-point match. The original image is the same as that in Fig. 7. The point-to-point matching is carried out between the predicted scattering center features and the scattering centers extracted as the local maximums in the image. There are altogether 48 scattering centers in the predicted feature, so we keep the largest 48 local maximums in the image. In the left subfigure, we can see that there is no obvious one-to-one correspondence between the two sets. On the contrary, the

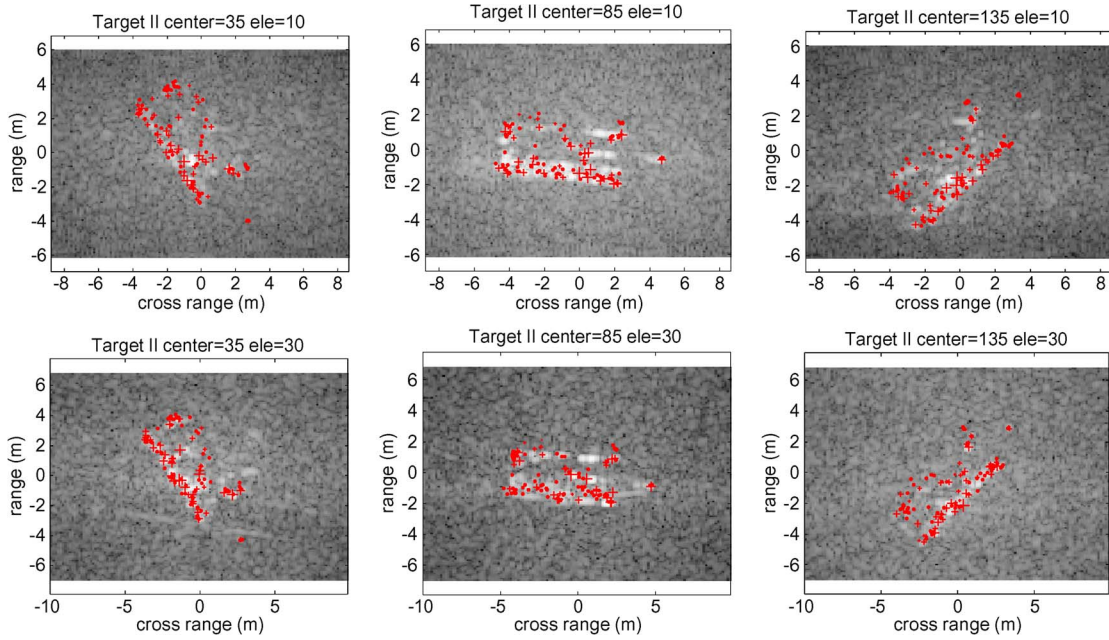


Fig. 11. Comparison between the predicted scattering center features and the images at different poses. The first row is for an elevation of 10° and azimuths of 35° , 85° , and 135° from left to right. The second row is for an elevation of 30° and azimuths of 35° , 85° , and 135° from left to right. The images are in decibel scale. The predicted 2-D scattering centers are marked by red “+,” with the size proportional to $A_k^{1/3}$. The scattering centers in the 3-D model, but not viewable in the imaging aperture, are marked by red points.

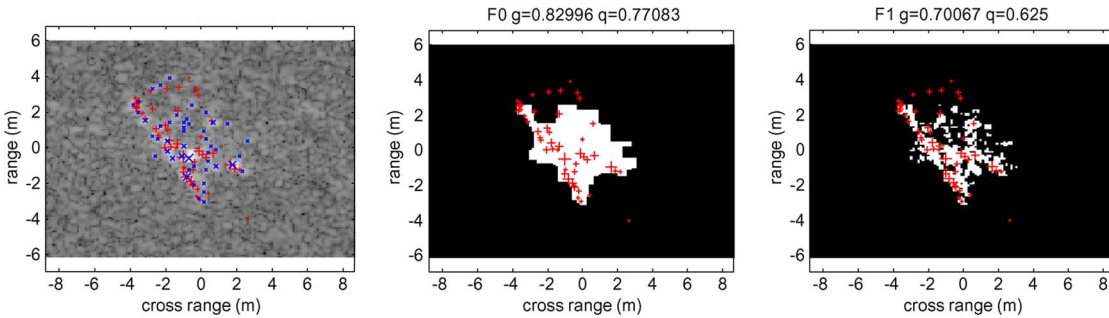


Fig. 12. Match between the predicted scattering centers and different image features for target II at an azimuth of 35° and an elevation of 10° . The image resolution is about $0.15 \text{ m} \times 0.15 \text{ m}$, and $\text{SNR} = 15 \text{ dB}$, as defined in (7). There are altogether 48 predicted scattering centers shown by red “+” in all of the three subfigures. (Left) Point-to-point match. Blue “x”s indicate the positions and amplitudes of the 48 scattering centers extracted from the image by local maximum test. The size of the cross is proportional to the cubic root of its amplitude. (Middle) Point-to-region match using F_0 , $g = 0.83$, and $q = 0.77$. (Right) Point-to-region match using F_1 , $g = 0.70$, and $q = 0.63$.

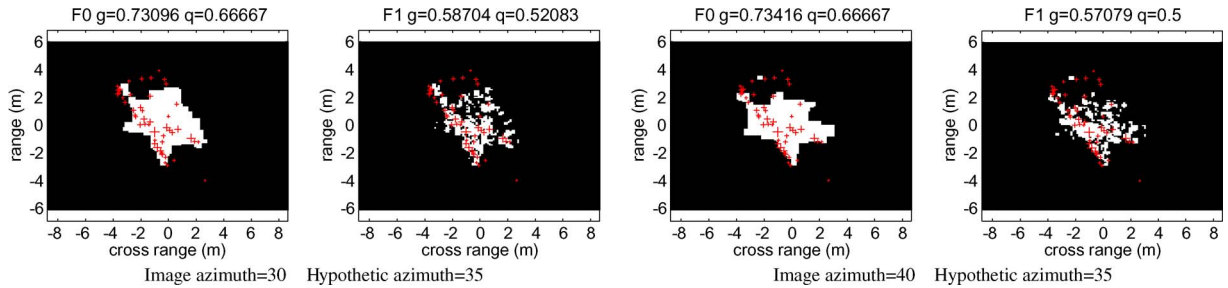


Fig. 13. Region-to-point match under pose estimation error. The scattering center features are predicted under the pose hypothesis of 35° . The images are at azimuth angles of 30° and 40° . (Left) Point-to-region match using F_0 with $+5^\circ$ pose estimation error. $g = 0.73$, and $q = 0.67$. (Middle left) Point-to-region match using F_1 with $+5^\circ$ pose estimation error. $g = 0.59$, and $q = 0.52$. (Middle right) Point-to-region match using F_0 with -5° pose estimation error. $g = 0.73$, and $q = 0.67$. (Right) Point-to-region match using F_1 with -5° pose estimation error. $g = 0.57$, and $q = 0.50$. The image resolution is about $0.15 \text{ m} \times 0.15 \text{ m}$, and $\text{SNR} = 15 \text{ dB}$, as defined in (7).

region-to-point matches in the middle and right subfigures are easy to calculate, and fairly good matching scores are obtained. 2) The region-to-point match is not sensitive to pose variation and noise. Fig. 13 shows the match between the predicted

scattering center feature and the extracted regional features under $\pm 5^\circ$ pose estimation errors. Comparing with Fig. 12, we can see that the matching scores decrease when there is pose estimation error, but the scores are still above the matching

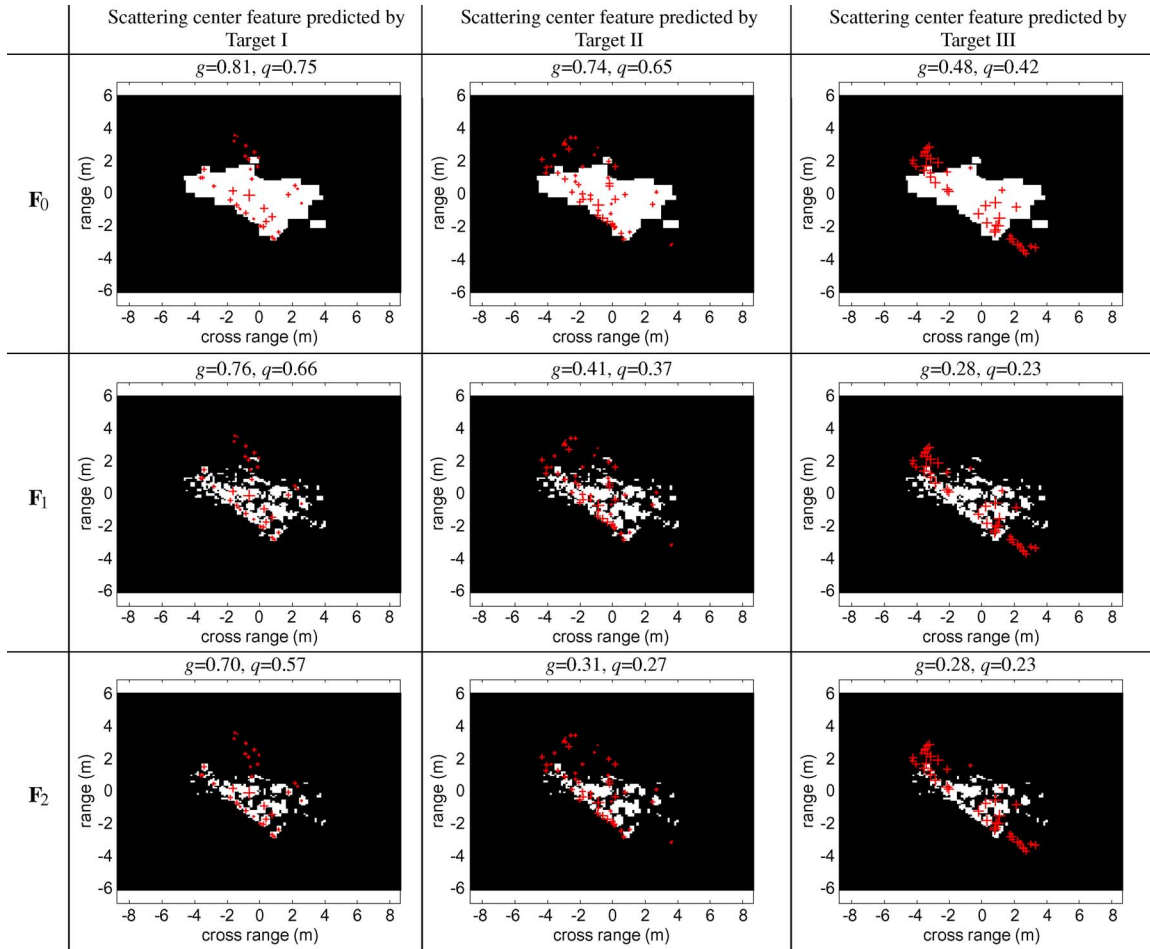


Fig. 14. Match between the regional features of target I and the scattering center features of different targets. The matching scores are given above each subfigure. The imaging and feature prediction poses are azimuth = 50° and elevation = 10° . The image resolution is about $0.15 \text{ m} \times 0.15 \text{ m}$, and SNR = 15 dB, as defined in (7).

thresholds defined in the next section. It is worth noting that the decrease in matching score using \mathbf{F}_0 is smaller than that using \mathbf{F}_1 . 3) Coarse regional features are more robust than fine regional features, and fine regional features in lower levels (i.e., with a smaller n) are more robust than in higher levels. This is partly demonstrated by the comparison between Figs. 12 and 13. Another example is shown in Fig. 14, which compares the matching scores of the same image with different target hypotheses. In Fig. 14, we can see that, although the correct target always gives the highest matching scores at different feature levels (this is not always true; otherwise, there will be no miss-classifications), the score differences among different target hypotheses are larger for finer features. Therefore, coarser features are less sensitive to both pose and target variations.

E. Decision Mechanism

The decision procedure is shown in Fig. 15. The considerations for this procedure can be summarized as follows: 1) if the test image can be matched with one of the targets in the library and differs with others markedly, it is reasonable to state that the test target belongs to this class. 2) The matching score difference obtained at a coarser level denotes more significant difference of the target with other targets in the library. This

is reasonable since coarser regional features are less sensitive to target variance. Therefore, the match is carried out in a test-and-repeat style starting from coarse regional feature and going through to finer features. If a significant matching score difference can be identified in one cycle, the decision can be made, and further tests using finer features are not necessary. This benefits the efficiency of the classifier. 3) Since coarser regional features are more robust than finer regional features, matching beginning from coarse regional features also benefits the robustness of the result. 4) It is not necessary to go to finer features if a satisfying matching score cannot be obtained at the current feature level because the matching score decreases as the feature level n increases. This benefits the efficiency of the classifier. 5) The matching scores must exceed certain thresholds before the decision is made so that wrong pose hypotheses will be rejected soon. This also benefits the robustness and efficiency of the classifier.

The decision criteria in Fig. 15 are decided based on the statistical properties of the matching scores. Fig. 16 shows the statistical distributions of the matching scores using \mathbf{F}_0 and \mathbf{F}_1 . At an elevation of 10° , 500 images of each target are produced, and the azimuths are randomly selected from $[15^\circ, 165^\circ]$ interval. The image resolution is about $0.15 \text{ m} \times 0.15 \text{ m}$, and the SNR is 10 dB, as defined in (7). In this experiment, we

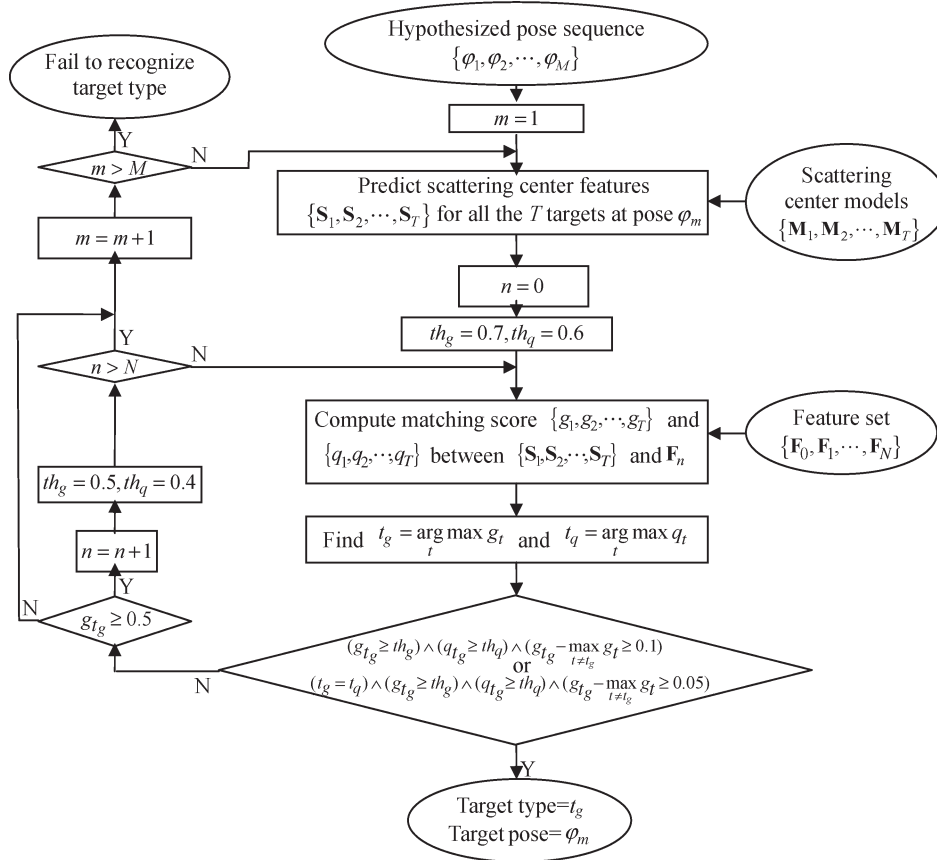


Fig. 15. Flowchart of the decision procedure.

do not take the pose estimation error into consideration. The \mathbf{F}_0 or \mathbf{F}_1 feature of each image is extracted and matched with the three candidate targets in the library, and the matching scores are labeled as g_1 – g_3 and q_1 – q_3 , respectively.

In Fig. 16, we can see that it is possible to define curved surfaces in any of the four subfigures to separate the three targets with high probability. That is to say, we need only one type of the matching scores (either g or q) and one level of the features if we just want to discriminate the three targets with enough training data. However, the decision criteria will be target dependent (note that the decision criteria in Fig. 15 remain unchanged for all of the targets in the library) and will be obscure in physical meaning. Therefore, we devise the rule-based hierarchical thresholding classifier in Fig. 15, with the expectation that a simpler classifier will have better adaptability. This advantage will be verified in Section V, where another target is added to the library without training data, and the decision criteria in Fig. 15 still work without any modifications.

IV. EXPERIMENTS USING SYNTHETIC DATA

In this section, we present some classification experiments using images computed by a high-frequency EM code as introduced in Section II.

The targets and their scattering center models are shown in Figs. 2 and 3. The test SAR images are obtained from the original data predicted by the same EM code. The computing

parameters are the following: frequency from 5 to 6 GHz, with a 12.5-MHz step; azimuth from 10° to 170° , with 0.1° interval; and elevation of 10° and 30° . Using the data, we can produce target images at any center azimuth in $[15^\circ, 165^\circ]$ with resolution up to $0.15 \text{ m} \times 0.15 \text{ m}$. Comparing with Section II, we can see that the azimuth grid points of the original data for model building are much sparser than that for imaging. The imaging steps include the following: 1) select data in a synthetic aperture, and add complex Gaussian white noise to achieve a certain SNR level; 2) interpolate the data from a sector to a rectangle in the spatial spectrum domain; 3) obtain image by 2-D FFT with zero-padding and Hamming windowing in both directions; and 4) map the image from the imaging plane to the ground plane by scaling the range axis by a factor of $1/\cos \gamma$ (γ is the elevation angle).

The SNR is defined as

$$\text{SNR (dB)} = 10 \log_{10} \frac{\sum_{i=1}^I \sum_{l=1}^L |x(i, l)|^2}{IL\sigma^2} \quad (7)$$

where $x(i, l)$ is the complex RCS predicted by the EM code at azimuth θ_i and frequency $f_0 + (l - 1)\Delta f$, $w(i, l) = n_R(i, l) + jn_I(i, l)$ is the noise added to $x(i, l)$, $n_R(i, l)$ and $n_I(i, l)$ are independent white Gaussian processes with variance $\sigma^2/2$, $y(i, l) = x(i, l) + w(i, l)$ is the data used for imaging, I is the number of angles in the aperture, and L is the number of frequencies in the band. Since noise is added independently in the spectrum domain, it will spread throughout the image, and

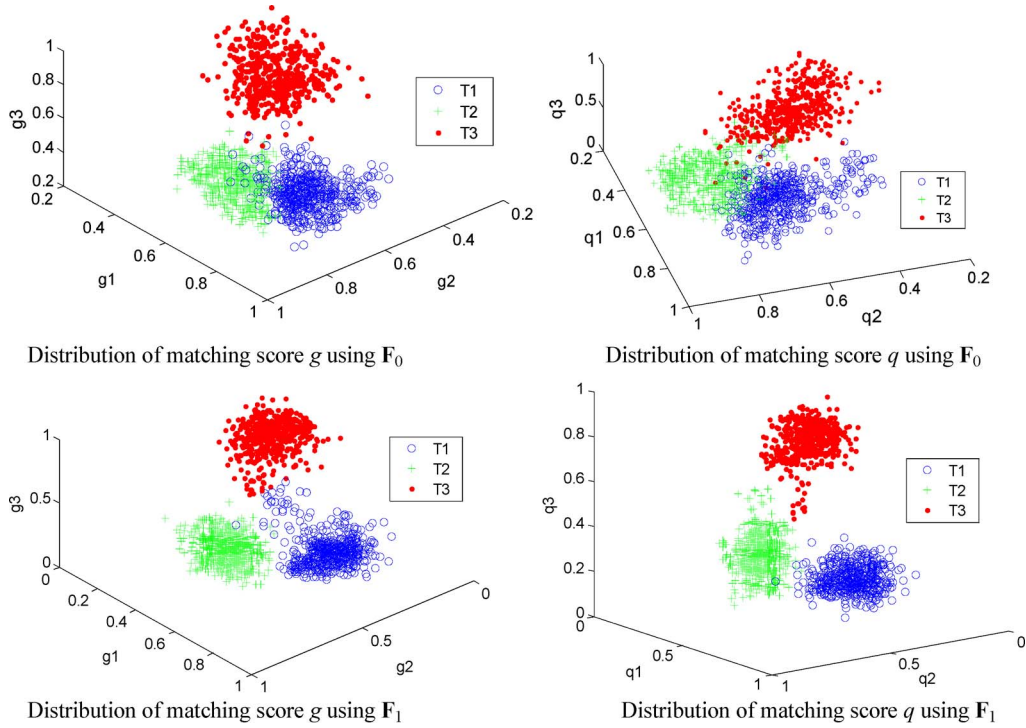


Fig. 16. Statistical distributions of matching scores using \mathbf{F}_0 and \mathbf{F}_1 . g_1 – g_3 and q_1 – q_3 are the matching scores with the three candidate targets in the library. At an elevation of 10° , 500 Monte Carlo simulations are carried out, and the azimuths are randomly selected from $[15^\circ, 165^\circ]$ interval. The image resolution is about $0.15 \text{ m} \times 0.15 \text{ m}$, and the SNR is 10 dB, as defined in (7).

there is no shadow behind the target. In field data comprised of backscattering from both the target and the ground, the shadow is also an important signature for ATR of ground targets [10].

In Sections IV-A and B, we use the data in the whole band and in an aperture of 10° for imaging. Therefore, $I = 101$, $L = 81$, and each image chip contains 128×128 pixels with a resolution of about $0.15 \text{ m} \times 0.15 \text{ m}$. The range and cross range resolutions in the ground plane should both be scaled by $1/\cos \gamma$ so that

$$\delta_{\text{xrange}} = \frac{\lambda}{2\Theta \cos \gamma} \quad \delta_{\text{range}} = \frac{c}{2B \cos \gamma}. \quad (8)$$

For cross range, it is caused by the reduction of the equivalent aperture in the spectrum domain, and for range, it is caused by the mapping from the imaging plane to the ground plane.

A. Classification Results of Three Targets

Fig. 17 shows the detailed classification results for target II at different azimuths. There are altogether five wrong decisions among the 151 tests, resulting in a recognition rate of 96.7%. In the bottom subfigure, we can see that most of the decisions can be made using \mathbf{F}_0 or \mathbf{F}_1 . This reflects the efficiency of the classifier. In the middle and bottom subfigures, we can see that, at most azimuths, the correct target pose (or with small error) is the first one in the pose sequence, and if it is not the first one, it can still be selected out by the classifier, as is the case for azimuths of 20° , 39° , 139° , 150° , etc.

Table I gives the statistical classification result (confusion matrix) for an elevation of 10° . The Monte Carlo experiments are carried out as follows. For each target, 500 azimuths are

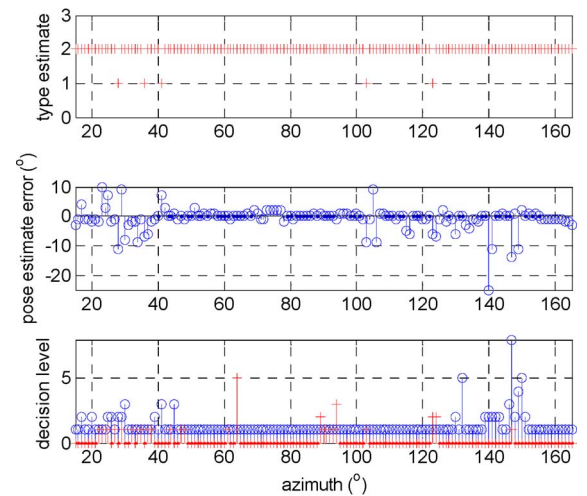


Fig. 17. Classification result for target II at different azimuths. Image resolution is about $0.15 \text{ m} \times 0.15 \text{ m}$, the SNR is 10 dB, and the elevation is 10° . The top subfigure is the decided target type at each azimuth. The middle subfigure is the difference between the pose estimate output by the classifier and the true pose. The bottom subfigure shows the index of the pose hypothesis m (blue circle) and the feature level n (red cross) when a decision is made.

TABLE I
CONFUSION MATRIX FOR THE THREE TARGETS IN FIG. 2 (500 MONTE CARLO SIMULATIONS, SNR = 10 dB, AND ELEVATION = 10°)

	Not identified	Target I	Target II	Target III
Target I	0	440	54	6
Target II	2	24	474	0
Target III	14	8	4	474

randomly selected with uniform distribution in interval $[15^\circ, 165^\circ]$. These azimuths are used as centers of a 10° aperture to produce SAR images. The image chips are then sent to the

TABLE II
CONFUSION MATRIX FOR THE THREE TARGETS IN FIG. 2 (500 MONTE CARLO SIMULATIONS, SNR = 10 dB, AND ELEVATION = 30°)

	Not identified	Target I	Target II	Target III
Target I	25	413	49	13
Target II	0	13	485	2
Target III	0	44	35	421

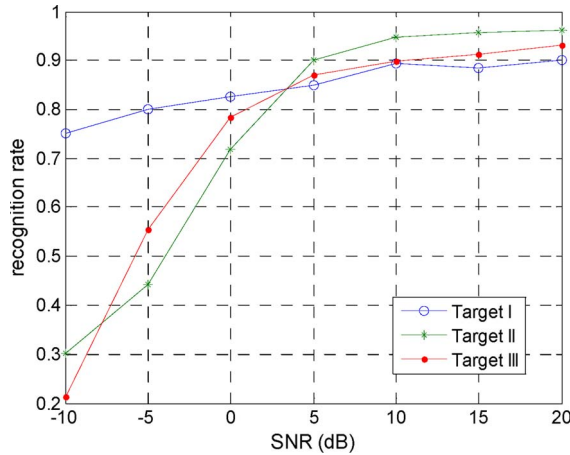


Fig. 18. Recognition rate for the three targets at different SNR levels.

classifier, and the classifying results are listed in Table I. The image resolution is about $0.15 \text{ m} \times 0.15 \text{ m}$, and the SNR is 10 dB. Table II is obtained similarly except that the elevation is 30°.

Tables I and II show that all of the three targets can be correctly identified with a probability higher than 80%. Comparing Tables I and II, we can see that the recognition rates for targets I and III decrease as the elevation increases from 10° to 30°. There may be two reasons for this phenomenon. One is that the image resolution in the ground plane decreases when the elevation increases. The other is that the difference in the projected shape and contour of different targets decreases as the elevation increases. The second reason may be confirmed from the results for target III whose shape differs obviously with the others (thinner and longer). Its probability to be confused with the other two targets increases obviously as the elevation increases from 10° to 30°. However, the recognition rate for target II increases a little as the elevation increases since it is less confused with target I. The reason may be that the structural difference (to be more specific, the difference in scattering structures) between the two targets is more obvious in the elevation direction than in the horizontal direction, as can be confirmed by Fig. 3 where the scattering structures rather than the geometric structures are presented.

We repeat the experiments in Tables I and II at different SNR levels. The relation between the classification results at elevations of 10° and 30° is similar to that in Tables I and II. Therefore, we add the results at the two elevations and divide them by 1000 to obtain the recognition rate. Fig. 18 shows the correct recognition rates for the three targets at different SNR levels. In Fig. 18, we can see that the classifier performs fairly well until the SNR falls beneath 5 dB. Targets II and III are apt to be confused with target I at low SNR (this is observed from the confusion matrices and is not shown in Fig. 18).



Fig. 19. CAD models for target II with different configurations. (Left) Shielded. (Middle) Fuel barrels removed. (Right) Gun turret rotated by 80°.

This is because the scattering center model for target I is the most concentrated one among the three (refer to Fig. 3). Therefore, its scattering center features are more concentrated and are apt to produce a higher matching score than the other two targets when the regional features are seriously distorted by noise. Although the recognition rate of target I remains comparatively high at low SNR, its false alarm rate is also high.

B. Classification Results of Target II in Various Conditions

One of the advantages of model-based ATR is its flexibility in extended operation conditions [14]. Therefore, we test our classifier in changed target configurations, which are instances of the extended operation conditions and which especially fit our method since the changes in target configurations can be conveniently reflected by the modifications of the scattering center model.

The CAD model of target II is modified in three different ways: 1) remove the lower part as if it were half shielded or buried; 2) remove the fuel barrels; and 3) rotate the gun turret by 80°. The scattering center model of target II can also be modified accordingly: 1) remove the scattering centers on the lower part; 2) remove the scattering centers on the fuel barrels; and 3) rotate the positions of the scattering centers on the gun turret, and modify their scattering coefficient matrices by $a'_k(\theta, \gamma) = a_k(|\theta - 80^\circ|, \gamma)$. This is only an approximation since the gun turret is not absolutely symmetric, and results will show that this approximation does help in improving recognition. Figs. 19 and 20 show the modified CAD models and the scattering center models.

Table III shows the classification result for target II with different configurations. The experiment is carried out in the same way as that for Table I except that the original data for imaging are now predicted by the EM code using the modified CAD models. The scattering center model is not modified accordingly, and we want to see how the configuration variations affect the classification results. The results for elevations of 10° and 30° are summed up in Table III. Comparing Table III with the summation of Tables I and II (only the result for target II is concerned), we can see that the recognition rate decreases when the target configuration varies from the standard configuration for model building. The decrease is most obvious for the turret rotated case, and this suggests that the turret is an important signature for classification.

The mismatch between the standard model and the varied target configurations can be partly amended by modifying the model, as is verified in Table IV. In this experiment, we use the correspondingly modified scattering center model of

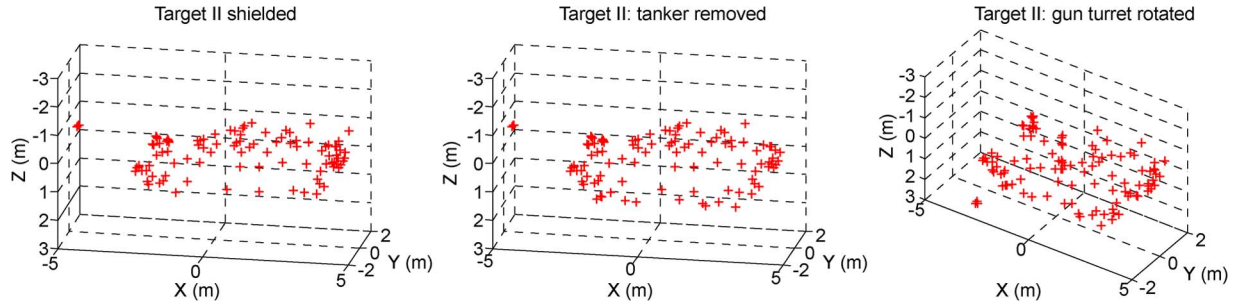


Fig. 20. Scattering center models of target II modified to reflect the changes in configurations. (Left) Shielded. (Middle) Fuel barrels removed. (Right) Gun turret rotated by 80° .

TABLE III
CLASSIFICATION RESULT FOR TARGET II WITH DIFFERENT CONFIGURATIONS. THE SCATTERING CENTER MODEL OF TARGET II IS NOT MODIFIED

	Not identified	Target I	Target II	Target III
Shielded	20	51	929	0
Fuel barrels removed	4	88	906	2
Gun turret rotated	66	117	817	0

TABLE IV
CLASSIFICATION RESULT FOR TARGET II WITH DIFFERENT CONFIGURATIONS. THE CORRESPONDINGLY MODIFIED SCATTERING CENTER MODEL OF TARGET II IS USED FOR EACH CONFIGURATION

	Not identified	Target I	Target II	Target III
Shielded	8	48	942	2
Fuel barrels removed	1	36	961	2
Gun turret rotated	55	58	887	0

target II for each configuration. Comparing Table IV with the summation of Tables I and II, we can see that, for both the shielded and fuel barrels removed case, the recognition rate is almost as good as in the standard operation condition. For the turret rotated case, however, model modifying helps in increasing the recognition rate, but it is still not as good as in the standard operation condition. The approximations in modifying the scattering coefficients may be one of the reasons.

C. Classification Results at Different Resolutions

This experiment is to test the performance of our method at different image resolutions. The images at lower resolution are obtained using a smaller aperture and a subband of the original data. The imaging steps are the same as that described at the beginning of this section. The accumulated SNR is used rather than the averaged SNR in (7) to avoid the variation of the accumulation gain at different resolutions. The accumulated SNR is defined as

$$SNR_{ac}(\text{dB}) = 10 \log_{10} \frac{\sum_{i=1}^I \sum_{l=1}^L |x(i, l)|^2}{\sigma^2}. \quad (9)$$

We set $SNR_{ac} = 55$ dB, which is about the same level as 15 dB in Fig. 18 for images at a resolution of $0.15 \text{ m} \times 0.15 \text{ m}$. It is worth noting that the peak SNR in an image will always be much smaller than that calculated by (9) since the target is not an ideal scatterer but contains tens of strong scatterers.

Fig. 21 shows the recognition rates for the three targets (target II is in its standard configuration) at resolutions from

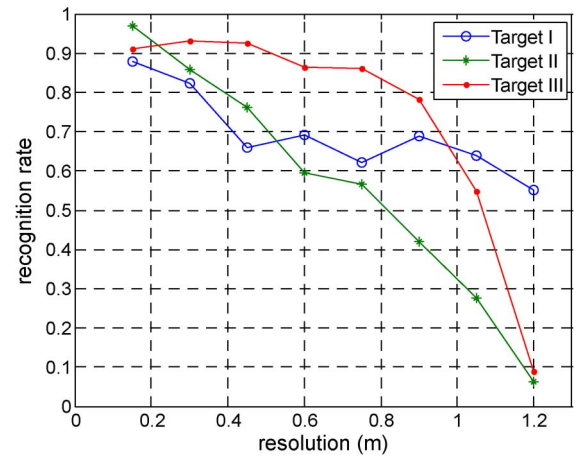


Fig. 21. Recognition rate for three targets at different resolutions.

$0.15 \text{ m} \times 0.15 \text{ m}$ to $1.2 \text{ m} \times 1.2 \text{ m}$. The classifier remains unchanged, except parameter S in Fig. 6, which is set empirically as $[800, 250, 100, 90, 75, 50, 30, 20]$, corresponding to the eight resolution levels. In Fig. 21, we can see that the classifier fails to distinguish the three targets when the resolution is worse than $0.6 \text{ m} \times 0.6 \text{ m}$. However, target III can still be discriminated from the other two by images with a resolution of $0.9 \text{ m} \times 0.9 \text{ m}$ (with both high correct recognition rate and low false alarm rate as observed from the confusion matrices not shown here). This is reasonable since target III differs obviously from the other two in size and shape, and these signatures are still kept by images with low resolution.

D. Scattering Center Registration

Until now, we have assumed perfect registration between the scattering center models and the images. In the previous simulations, the CAD models used to compute the imaging data and the 3-D scattering center models share the same coordinate system so that the origins of the images and the projected 2-D scattering centers coincide. However, if the detection stage has image extraction errors in the presence of ground clutter, coordinate offsets will occur. Therefore, the scattering center features must be registered to the images before region-to-point matching since this matching has little translation invariance, as we will show soon.

Although the original scattering center models are 3-D, the registration has to be carried out for their 2-D projections since the test images are 2-D. Correlation is a classical approach

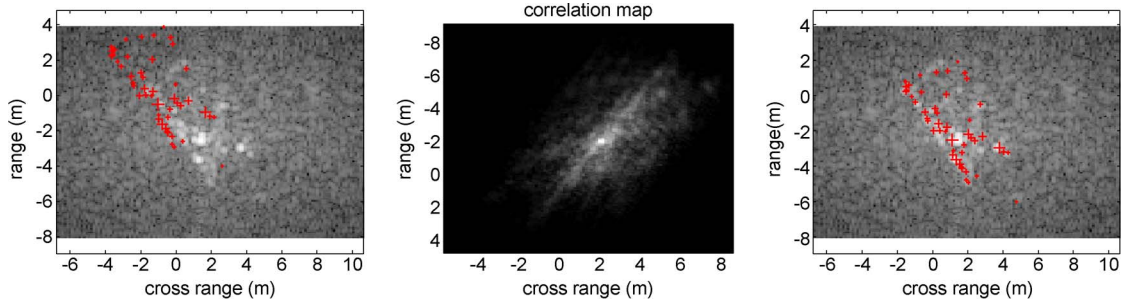


Fig. 22. Example of registration between the image and the projected scattering centers. (Left) Shifted image of target II and the original scattering centers. (Middle) Correlation map between the images in F_1 and the scattering centers. (Right) Scattering centers registered to the image.

for registration, and the 2-D correlation between two images is computationally intensive. However, in our application, the correlation is carried out between an image and several points. The 2-D correlation manipulation can be simplified to several shifting and adding manipulations if we view the 2-D scattering centers as a 2-D function composed of several 2-D Diracs. Moreover, the scattering centers are registered not to the whole image but to the image in the F_1 region. This will not only decrease the effect of the noise but also reduce the computing load even more. Also, we use the cubic root of the image amplitude and the cubic root of the scattering center intensity to weaken the dominating effects of some very strong scatterers.

Denoting the cubic root of the amplitude image in the F_1 region as $Y_1(m, n)$ and the projected 2-D scattering centers as $Y_2(m, n)$, we have

$$Y_2(m, n) = \sum_{k \in \kappa(\theta, \gamma)} A_k^{1/3} \delta(m - \text{round}(x_k''/\Delta x)) \times \delta(n - \text{round}(y_k''/\Delta y)) \quad (10)$$

where $\kappa(\theta, \gamma)$ and (x_k'', y_k'', A_k) are defined in (3)–(5) and Δx and Δy are the image pixel sizes in the range and cross range dimensions, respectively. The coordinates of the scattering centers are discretized to the nearest image pixels so that the shifting manipulation in the following will be feasible for the discrete image. The correlation between $Y_1(m, n)$ and $Y_2(m, n)$ can be calculated as

$$\begin{aligned} C_{Y_1 Y_2}(m, n) &= \sum_{m'} \sum_{n'} Y_1(m' + m, n' + n) Y_2(m', n') \\ &= \sum_{k \in \kappa(\theta, \gamma)} A_k^{1/3} Y_1(\text{round}(x_k''/\Delta x) + m, \\ &\quad \text{round}(y_k''/\Delta y) + n). \end{aligned} \quad (11)$$

This is easily carried out by shifting $Y_1(m, n)$ several times and by adding these shifted chips together. Then, the offsets in both directions can be estimated as

$$\{m_0, n_0\} = \arg \max_{\{m, n\}} C_{Y_1 Y_2}(m, n). \quad (12)$$

The scattering centers can be registered to the image by

$$x_k''' = x_k'' + m_0 \Delta x \quad y_k''' = y_k'' + n_0 \Delta y. \quad (13)$$

Therefore, the 2-D scattering center feature S used in Fig. 15 should be $S = \{(x_k''', y_k''', A_k), k \in \kappa(\theta, \gamma)\}$ instead of the original one introduced in Section III-C.

Fig. 22 shows an example of the registration procedure. The original image is the same as that in Figs. 7 and 9: target II at an elevation of 10° and an azimuth of 35° , with a resolution of $0.15 \text{ m} \times 0.15 \text{ m}$ and an SNR of 15 dB. The only difference is that now the center of the image is shifted from $(0, 0)$ to $(2, -2)$ so that the original scattering centers cannot correspond well with the image in the left subfigure. The middle subfigure is the correlation map calculated using (11), and we can see that the maximum appears at about $(2, -2)$. Therefore, we shifted the scattering centers according to (13), and the result in the right subfigure shows that now the shifted scattering centers correspond well with the image.

Fig. 23 tests the translational invariance of the classifier with and without the registration step. The settings for this experiment are similar to that in Fig. 18 except that here we set SNR = 10 dB and shift the image chips with an offset uniformly distributed in $[-d, d]$ in both range and cross range directions. We vary d from 0 to 1 m and calculate the recognition rate at each shift range. The left subfigure is the result for the classifier in Fig. 15. We can see that the recognition rate decreases fast when the shift range increases, and this indicates that the region-to-point matching has little translational invariance. Therefore, a registration step must be added after the second step in the main flow of Fig. 15, i.e., it is carried out outside the feature level cycle and inside the pose hypothesis cycle. The recognition performance of this modified classifier is shown in the right subfigure. There are only small random variations for the recognition rates at different shift ranges. Comparing the right subfigure with the left subfigure, we can see that the performance of the modified classifier is similar to that of the original classifier with a shift range of 0.2–0.3 m. This is reasonable since the offsets estimated by (13) are discretized by pixel size (which is slightly smaller than 0.15 m in this experiment), so the estimation error of 1–2 pixels will cause a residual registration error at this magnitude.

V. EXPERIMENTS USING FIELD DATA

In this section, some of the MSTAR public data are used to test the classifier. We acquire the MSTAR image chips of a T-72 tank at an elevation of 17° . There are altogether three groups of data chips named as SN_132, SN_812, and SN_S7. Since the T-72 scattering center model introduced in the next paragraph

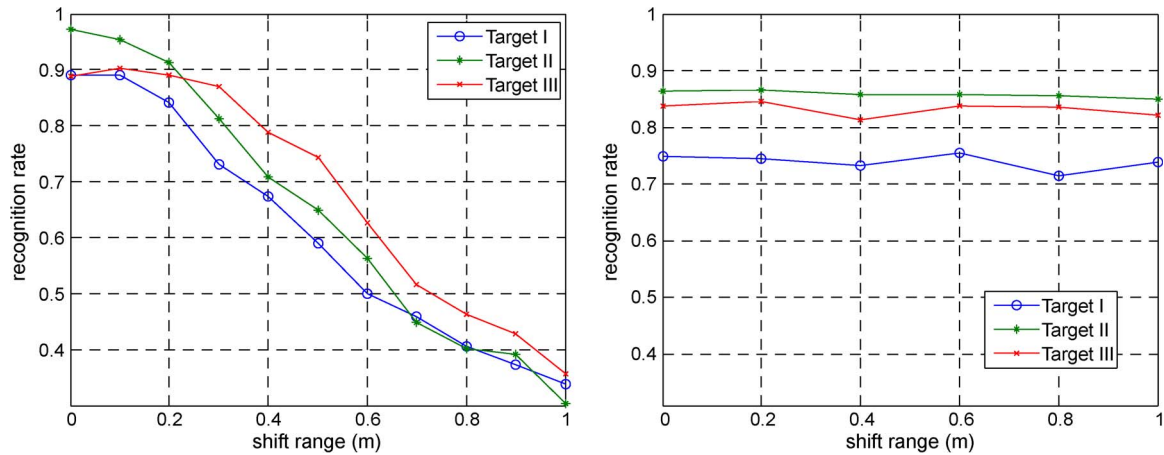


Fig. 23. Recognition performance of the classifier with different image shift ranges. (Left) There is no registration step in the classifier. (Right) Registration step is added in the classifier.

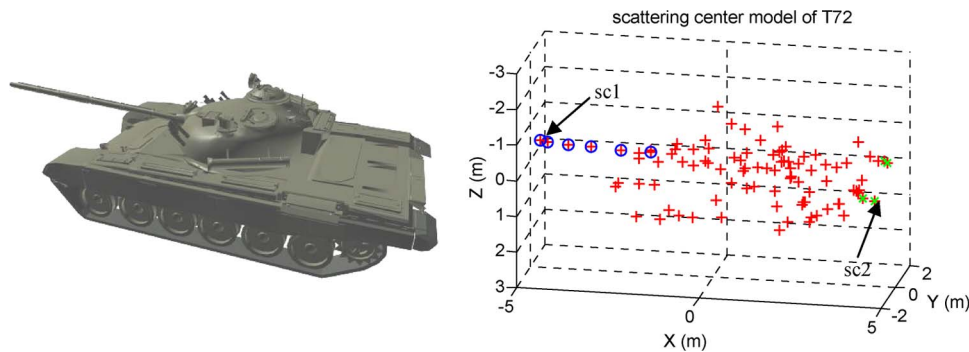


Fig. 24. Models of a T-72 tank. (Left) CAD model. (Right) Scattering center model with altogether 94 scattering centers.

is built for the azimuth interval $[0^\circ, 180^\circ]$, only the image chips with the recorded target azimuth in $[0^\circ, 180^\circ]$ are used as test images (note that the recorded azimuth cannot be used to replace the pose estimation step). Therefore, the numbers of the test images in the three data sets are 118, 119, and 106, respectively.

To implement the classifier, we must build the 3-D scattering center model of the T-72 tank. We use a commercial CAD model of the tank, as shown in the left subfigure of Fig. 24. The original data used for model building are computed by the same EM code as that used in Section II with the following parameters: frequency from 5 to 6 GHz, with a 12.5-MHz step; azimuth from 0° to 180° , with 1° interval; and elevation from 4° to 45° , with 1° interval. Note that the MSTAR data are measured using an X-band radar, but we compute the model building data in the C-band to save the EM computing time, and the results will show that such a model is acceptable. This verifies one of the advantages of the scattering center model as stated in Section II: it is not sensitive to radar parameters such as center frequency and bandwidth. There are altogether 94 scattering centers in the model, as shown in the right subfigure of Fig. 24. We mark out the scattering centers on the gun by blue circles and the scattering centers on the trail baffle by green crosses. The effects of these scattering centers on the recognition performance will be investigated in the experiments.

Fig. 25 shows the scattering coefficients (amplitude in decibel scale) of the first and second scattering centers identified in

the right subfigure of Fig. 24. These two scattering centers are on the gun and trail baffle, respectively. Fig. 25 will be revisited in the following discussions.

Now, we give some image chips from the MSTAR data and investigate how well they correspond with the scattering center model built from the EM data. Fig. 26 shows three image chips overlaid by the projected scattering centers. The scattering centers have been registered to the image using the algorithm described in Section IV-D. In Fig. 26, we can see that most of the scattering centers lie in the bright regions in the images. However, there are exceptions: 1) the strong glint of the gun when irradiated by the perpendicular radar LOS (please refer to the middle subfigure) is not predicted by the scattering center model (please refer to the left subfigure of Fig. 25). This is reasonable since the model only contains the stable scattering centers, whereas the mirror reflection is an instantaneous one existing in a very small angular extent. However, in other poses, the scattering centers on the gun are always viewable in the scattering center model (please refer to the left subfigure of Fig. 25), but the gun is seldom evident in the image chips. 2) According to the scattering center model, the scattering centers on the trail baffle are viewable at azimuths larger than 100° (please refer to the right subfigure of Fig. 25), but there are no corresponding peaks in the image chips. This mismatch may be caused by some configuration variations of the target. Although not sure about the specific configurations, we will consider removing these scattering centers to better fit the scene.

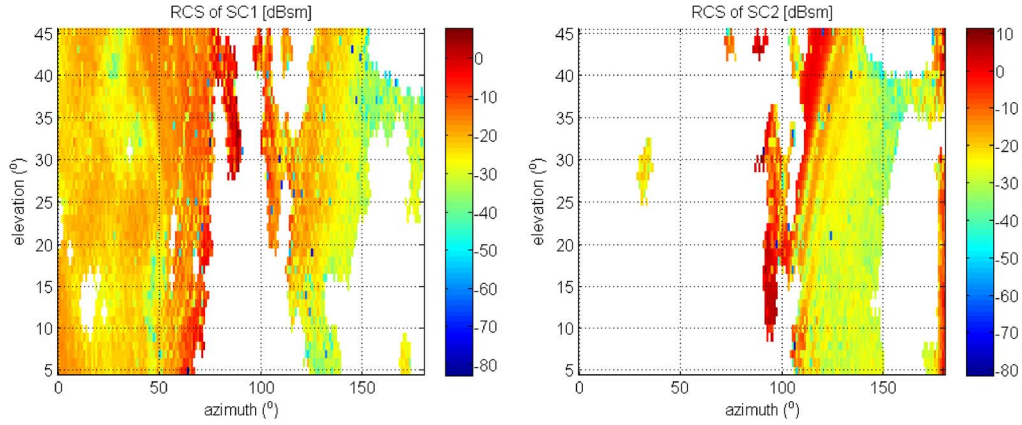


Fig. 25. Scattering amplitudes (in decibel scale) at different azimuth and elevation angles of the first and second scattering centers in the T-72 model. (Left) Scattering center 1. (Right) Scattering center 2.

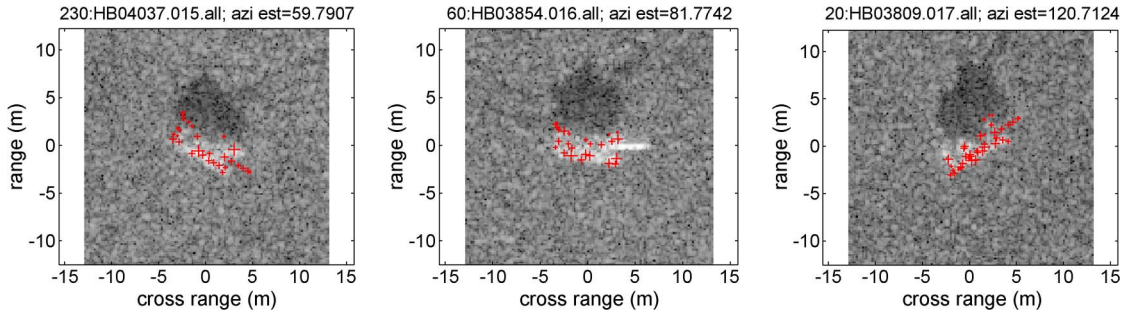


Fig. 26. Comparison between the predicted scattering center features and the images at different poses. The images are in decibel scale, and the scattering centers are marked by “+,” with the size proportional to the cubic root of the amplitude. The target azimuths in the subfigures from left to right are 59.8°, 81.8°, and 120.7°, respectively.

TABLE V
CLASSIFICATION RESULTS OF THE MSTAR T-72 DATA SETS AT 17° ELEVATION. ONLY IMAGE CHIPS IN [0°, 180°] AZIMUTH ARE TESTED. TWO T-72 SCATTERING CENTER MODELS WITH DIFFERENT CONFIGURATIONS ARE USED SEPARATELY

Dataset	T-72 scattering center model configuration	Classification Results (with correct classification rate in the parentheses)				
		T-72	Target I	Target II	Target III	Not identified
SN_132 (118 test images)	Original	25 (21.2%)	34	35	10	2
	Gun and baffle removed	91 (77.1%)	9	7	11	0
SN_812 (119 test images)	Original	35 (29.4%)	39	39	6	0
	Gun and baffle removed	103 (86.6%)	3	10	3	0
SN_S7 (106 test images)	Original	24 (22.6%)	37	37	7	1
	Gun and baffle removed	87 (82.1%)	8	8	2	1

Table V shows the classification results for the image chips in group SN_132, SN_812, and SN_S7, respectively. The candidate targets in the library include the three targets used in the previous section (target II in its standard configuration) and the T-72 model in Fig. 24. It is worth noting that the size of target II (length of 9.66 m, width of 3.60 m, and height of 2.20 m) is very similar to that of the T-72 (length of 9.45 m, width of 3.38 m, and height of 2.19 m). We separately test two configurations of the T-72 scattering center model according to the aforementioned analysis: the original scattering center model shown in the right subfigure of Fig. 24 and the modification of the original scattering center model by removing ten scattering centers (four on the trail baffle and six on the gun).

It is worth noting that the S parameter used in the regional feature extraction (please refer to Fig. 6) is set as 350 since the pixel size in the image chips is about

0.2 m \times 0.2 m, and a registration step is added as explained in Section IV-D. All of the other parameters of the classifier remain unchanged.

Comparing the two rows for each data set, we find that the scattering center adjustment significantly improves the recognition performance. This indicates that the extended operation conditions will be better suited by adjusting the scattering center models, even if the adjustments can only approximate the target configuration variations. Comparing the results for the three data sets, we find that the classifier performs best for data set SN_812 (86.6%), then data set SN_S7 (82.1%), and data set SN_132 at the last (77.1%). Explanations of these results will need further knowledge of the data acquisition conditions.

Compared with the classifiers developed in the MSTAR project [9], the classification rates in Table V are not high even after model modification. The fidelity of the scattering

center model may be an important reason. Besides the model building procedure, there are other factors that can improve the fidelity of the scattering center model: 1) using a CAD model of higher fidelity; 2) including more scattering mechanisms in the EM predicting code; 3) including the interaction between the ground and the target in the scattering model; and 4) designing an intelligent scheme to adjust the configuration hypotheses (such as the local search step in [11]) to obtain proper scattering center model modifications. Also, the classification performance may be increased by exploring other features in the image chips such as shadows, ridges, and edges [10] besides the peaks. Therefore, the experiments in this section only provide a preliminary verification of our classifier, and future work is demanded to provide an integrated solution to SAR ATR based on it.

VI. DISCUSSIONS

This paper has proposed a SAR image classification method based on global scattering center models. The main advantages of this method include the following: small data amount for model building and storing, fast and flexible feature prediction, and fast image feature extraction and image-model matching.

Although we have taken much effort to test its performance in different conditions, there is still much work to do, especially in improving the method according to the characters of the field data. Two important differences between the EM code predicting data and the field data are the following: 1) the dihedral formed by the ground and the target's side plate will produce strong backscattering and will form new scattering centers in the model, and 2) the target shadow in the ground clutter is also an important signature for target classification. In the experiments of Section V, these two characteristics are not considered both in model building and in image feature extraction. Therefore, the performance can be improved if we exploit the special characteristics. The problem is how to integrate these considerations into the scattering-center-model-based classification frame.

There are still other points to be refined in our method. For example, the scattering center model can be modified to suit the configuration variation. But how will we know the specific configuration beforehand, or is there any other way to instruct the modification of the scattering center model? Further work on this method will be carried on to realize its attractive potential in application.

APPENDIX

FUNDAMENTAL MORPHOLOGICAL OPERATIONS

A binary image in the n -dimensional Euclidean space E^n can be denoted by a set in this space. Supposing that A and B are two sets in E^n , the dilation $A \oplus B$ is defined as

$$A \oplus B = \{c \in E^n | c = a + b, a \in A, b \in B\}. \quad (A1)$$

The erosion $A \ominus B$ is defined as

$$A \ominus B = \{c \in E^n | c + b \in A, \forall b \in B\}. \quad (A2)$$

The opening of the binary image A by the structuring element B is denoted by $A \circ B$ and is defined as

$$A \circ B = (A \ominus B) \oplus B. \quad (A3)$$

The closing of the binary image A by the structuring element B is denoted by $A \bullet B$ and is defined as

$$A \bullet B = (A \oplus B) \ominus B. \quad (A4)$$

ACKNOWLEDGMENT

The authors would like to thank the EMC Laboratory, Beijing University of Aeronautics and Astronautics, Beijing, China, for providing the high-frequency EM code and the anonymous reviewers for their detailed and helpful comments which significantly improved the quality of this paper.

REFERENCES

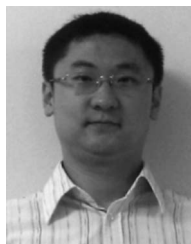
- [1] J. A. Richards, "Target model generation from multiple synthetic aperture radar images," Ph.D. dissertation, Dept. Electron. Eng. Comput. Sci., MIT, Cambridge, MA, 2001.
- [2] L. M. Novak, G. J. Owirka, W. S. Brower, and A. L. Weaver, "The automatic target-recognition system in SAIP," *Lincoln Lab. J.*, vol. 10, no. 2, pp. 187–202, 1997.
- [3] L. M. Novak, G. J. Owirka, and W. S. Brower, "Performance of 10- and 20-target MSE classifiers," *IEEE Trans. Aerosp. Electron. Syst.*, vol. 36, no. 4, pp. 1279–1289, Oct. 2000.
- [4] L. M. Novak, S. D. Halversen, G. Owirka, and M. Hiett, "Effects of polarization and resolution on SAR ATR," *IEEE Trans. Aerosp. Electron. Syst.*, vol. 33, no. 1, pp. 102–116, Jan. 1997.
- [5] Y. Chen, E. Blasch, T. Qian, and E. Blasch, "Experimental feature-based SAR ATR performance evaluation under different operational conditions," in *Proc. 17th SPIE—Signal Processing, Sensor Fusion, and Target Recognition*, May 2008, vol. 6968, pp. 69680F-1–69680F-12.
- [6] J. A. O'Sullivan, M. D. DeVore, V. Kedia, and M. I. Miller, "SAR ATR performance using a conditionally Gaussian model," *IEEE Trans. Aerosp. Electron. Syst.*, vol. 37, no. 1, pp. 91–108, Jan. 2001.
- [7] K. Copesey and A. Webb, "Bayesian gamma mixture model approach to radar target recognition," *IEEE Trans. Aerosp. Electron. Syst.*, vol. 39, no. 4, pp. 1201–1217, Oct. 2003.
- [8] M. D. DeVore and J. A. O. Sullivan, "Performance complexity study of several approaches to automatic target recognition from SAR images," *IEEE Trans. Aerosp. Electron. Syst.*, vol. 38, no. 2, pp. 632–648, Apr. 2002.
- [9] R. Hummel, "Model-based ATR using synthetic aperture radar," in *Proc. IEEE Int. Radar Conf.*, 2000, pp. 856–861.
- [10] J. Douglas, M. Burke, and G. Ettinger, "High resolution SAR ATR performance analysis," in *Proc. 11th SPIE—Algorithms Synthetic Aperture Radar Imagery*, Sep. 2004, vol. 5427, pp. 293–301.
- [11] J. R. Diemunsch and J. Wissinger, "Moving and stationary target acquisition and recognition (MSTAR) model-based automatic target recognition: Search technology for a robust ATR," in *Proc. 5th SPIE—Algorithms Synthetic Aperture Radar Imagery*, Sep. 1998, vol. 3370, pp. 481–492.
- [12] G. Jones and B. Bhanu, "Recognition of articulated and occluded objects," *IEEE Trans. Pattern Anal. Mach. Intell.*, vol. 21, no. 7, pp. 603–613, Jul. 1999.
- [13] B. Bhanu and Y. Q. Lin, "Stochastic models for recognition of occluded targets," *Pattern Recognit.*, vol. 36, no. 12, pp. 2855–2873, Dec. 2003.
- [14] T. D. Ross, J. J. Bradley, L. J. Hudson, and M. P. O'Connor, "SAR ATR: So what's the problem?—An MSTAR perspective," in *Proc. 6th SPIE—Algorithms Synthetic Aperture Radar Imagery*, Apr. 1999, vol. 3721, pp. 662–672.
- [15] G. Margarit, J. J. Mallorquí, and X. Fàbregas, "Single-pass polarimetric SAR interferometry for vessel classification," *IEEE Trans. Geosci. Remote Sens.*, vol. 45, no. 11, pp. 3494–3502, Nov. 2007.
- [16] G. Margarit, J. J. Mallorquí, J. Fortuny-Guasch, and C. Lopez-Martinez, "Exploitation of ship scattering in polarimetric SAR for an improved classification under high clutter conditions," *IEEE Trans. Geosci. Remote Sens.*, vol. 47, no. 4, pp. 1224–1235, Apr. 2009.

- [17] M. Martorella, E. Giusti, L. Demi, Z. Zhou, A. Cacciamano, F. Berizzi, and B. Bates, "Target recognition by means of polarimetric ISAR images," *IEEE Trans. Aerosp. Electron. Syst.*, vol. 47, no. 1, pp. 225–239, Jan. 2011.
- [18] J. Zhou, H. Zhao, Z. Shi, and Q. Fu, "Global scattering center model extraction of radar targets based on wideband measurements," *IEEE Trans. Antennas Propag.*, vol. 56, no. 7, pp. 2051–2060, Jul. 2008.
- [19] R. Bhalla, H. Ling, J. Moore, D. J. Andersh, S. W. Lee, and J. Hughes, "3D scattering center representation of complex targets using the shooting and bouncing ray technique: A review," *IEEE Antennas Propag. Mag.*, vol. 40, no. 5, pp. 30–39, Oct. 1998.
- [20] D. G. Arnold and R. Claypool, "Synthesizing invariant 3-D rigid scattering centers," *Proc. SPIE*, vol. 4382, pp. 395–403, 2001.
- [21] L. C. Potter and R. L. Moses, "Attributed scattering centers for SAR ATR," *IEEE Trans. Image Process.*, vol. 6, no. 1, pp. 79–91, Jan. 1997.
- [22] M. Martorella, E. Giusti, A. Capria, F. Berizzi, and B. Bates, "Automatic target recognition by means of polarimetric ISAR images and neural networks," *IEEE Trans. Geosci. Remote Sens.*, vol. 47, no. 11, pp. 3786–3794, Nov. 2009.
- [23] J. M. Rius, M. Ferrando, and L. Jofre, "GRECO: Graphical electromagnetic computing for RCS prediction in real time," *IEEE Antennas Propag. Mag.*, vol. 35, no. 2, pp. 7–17, Apr. 1993.
- [24] G. Margarit, J. J. Mallorqui, J. M. Rius, and J. Sanz-Marcos, "On the usage of GRECOSAR, an orbital polarimetric SAR simulator of complex targets, to vessel classification studies," *IEEE Trans. Geosci. Remote Sens.*, vol. 44, no. 12, pp. 3517–3526, Dec. 2006.
- [25] L. I. Voicu, R. Patton, and H. R. Myler, "Multi-criterion vehicle pose estimation for SAR ATR," in *Proc. 6th SPIE—Algorithms Synthetic Aperture Radar Imagery*, Apr. 1999, vol. 3721, pp. 497–506.



Shi Zhiguang was born in Shandong, China, in 1975. He received the B.E. degree in automatic control from Shijiazhuang Mechanical Engineering College, Shijiazhuang, China, in 1996 and the M.E. and Ph.D. degrees in information and telecommunication systems from the National University of Defense Technology (NUDT), Changsha, China, in 2002 and 2007, respectively.

He is currently a Lecturer with the ATR Laboratory, NUDT. His research interest includes clutter modeling and statistical analysis.



Cheng Xiao was born in Dalian, China, in 1983. He received the B.E. and M.Eng.Sc. degrees from the National University of Defense Technology, Changsha, China, in 2004 and 2009, specializing in automatic target recognition.

He is currently an Engineer with the Beijing Aerospace Control Center, Beijing, China. His current research activity focuses on spaceflight TT and C systems.



Zhou Jianxiong was born in Xiangtan, China, in 1977. She received the B.E. degree in electronics and the M.E. and Ph.D. degrees in information and telecommunication systems from the National University of Defense Technology (NUDT), Changsha, China, in 2000, 2002, and 2006, respectively.

She is currently a Vice Professor with the ATR Laboratory, NUDT. Her research interest includes target characteristics and radar signal processing.



Fu Qiang was born in Changsha, China, in 1962. He received the B.E. degree in electronics engineering and the Ph.D. degree in information and telecommunication systems from the National University of Defense Technology (NUDT), Changsha, in 1983 and 2004.

He is currently a Professor with the ATR Laboratory, NUDT. His research interest includes radar system design, precise guidance, and target recognition.